

Vorticity-induced negative nonlocal resistance in a viscous two-dimensional electron systemA. D. Levin,¹ G. M. Gusev,¹ E. V. Levinson,¹ Z. D. Kvon,^{2,3} and A. K. Bakarov^{2,3}¹*Instituto de Física da Universidade de São Paulo, 135960-170, São Paulo, SP, Brazil*²*Institute of Semiconductor Physics, Novosibirsk 630090, Russia*³*Novosibirsk State University, Novosibirsk 630090, Russia*

(Received 10 April 2018; revised manuscript received 6 June 2018; published 25 June 2018)

We report nonlocal electrical measurements in a mesoscopic size two-dimensional (2D) electron gas in a GaAs quantum well in a hydrodynamic regime. Viscous electric flow is expected to be dominant when electron-electron collisions occur more often than the impurity or phonon scattering events. We observe a negative nonlocal resistance and attribute it to the formation of whirlpools in the electron flow. We use the different nonlocal transport geometries and compare the results with a theory demonstrating the significance of hydrodynamics in mesoscopic samples.

DOI: [10.1103/PhysRevB.97.245308](https://doi.org/10.1103/PhysRevB.97.245308)**I. INTRODUCTION**

It is generally believed that, in the absence of disorder, a many-body electron system resembles the viscous flow. Hydrodynamic characteristics can be specially enhanced in a pipe flow setup, where the mean free path for electron-electron collision l_{ee} is much shorter than the sample width W , while the mean free path due to impurity and phonon scattering l is larger than W . Viscosity is characterized by momentum relaxation in the fluid and, in narrow samples, occurs at the sample boundary. Calculation of the shear viscosity η is a difficult task because it requires knowledge of particle interactions on the scale of l [1].

It has been predicted that the resistivity of metals in the hydrodynamic regime is proportional to electron shear viscosity $\eta = \frac{1}{4}v_F^2\tau_{ee}$, where v_F is the Fermi velocity and τ_{ee} is the electron-electron scattering time $\tau_{ee} = l_{ee}/v_F$ [2–6]. This dependency could lead to interesting properties. For example, resistance decreases with the square of temperature $\rho \sim \eta \sim \tau_{ee} \sim T^{-2}$, the so called Gurzhi effect, and with the square of sample width $\rho \sim W^{-2}$. The negative differential resistance has been observed previously in GaAs wires, which has been interpreted as the Gurzhi effect due to heating by the current [7]. A remarkable manifestation of the hydrodynamic effect is a swirling feature in the flow field, referred to as a vortex. The vorticity can drive the current against an applied electric field and generate backflow near the current injection region, which can be detected in the experiment as a negative voltage drop [8]. A different transport measurement setup has been proposed for the identification of viscosity related features in the hydrodynamic regime [8–11].

When fluid flows along a pipe, a quadratical velocity profile is formed, which leads to the Gurzhi effect, and can be detected from the anomalous temperature and sample width dependence, as is mentioned above. For illustration we modeled the Poiseuille flow for a two-dimensional neutral fluid. Figure 1(a) shows the configuration, which has been proposed in [8], and where the current is injected across the sample between vertical probes. In this geometry, one can see the vortex or whirlpools in the liquid flow outside of the main current path.

As a consequence, for an electronic fluid, a negative voltage drop occurs across the strip in close proximity to the current probes. Figure 1(b) illustrates the nonlocal, vicinity transport geometry, where the current is injected in the left lateral and bottom contacts, while the voltage drop occurs near the current injection region. This geometry has been proposed in [9–11], and the model clearly demonstrates the formation of whirlpools in the hydrodynamic flow, yielding a negative nonlocal signal in transport measurements [11]. Note that the swirling features can be observed only in the nonlocal configuration.

The nonlocal vicinity effect has been studied experimentally in an ultraclean graphene sheet [11]. It has been demonstrated that the nonlocal signal undergoes a sign change from positive, at low temperatures, to negative, above elevated temperatures, that is associated with whirlpool emergence in the hydrodynamic regime. Near room temperature, the signal again undergoes a sign change because the Ohmic contribution starts to dominate the vicinity response at high T . Note that such dramatic experimental appearance of hydrodynamic features in nonlocal transport has not been accompanied by observation of the Gurzhi effect in local transport. Moreover, the transversal nonlocal geometry (Fig. 1) has not been studied experimentally with respect to possible vorticity effects. Other materials, such as GaAs quantum wells, have a particular interest because they possess the highest mobility over wide temperature ranges. It is also worthwhile to extend the theoretical approach [8–11] to a two-dimensional electron in GaAs with a parabolic energy spectrum, which is different from the linear spectrum in graphene.

A series of updated theoretical approaches has been published recently [12–15], providing additional possibilities to determine the viscosity from magnetotransport measurements, which can be used for comparison with nonlocal measurements.

In this study we measure the nonlocal resistance in mesoscopic GaAs quantum well systems. We determine all relevant electron viscous parameters from the longitudinal magnetoresistance in a wide temperature range, which provides an estimate of the nonlocal signal, and compare it with

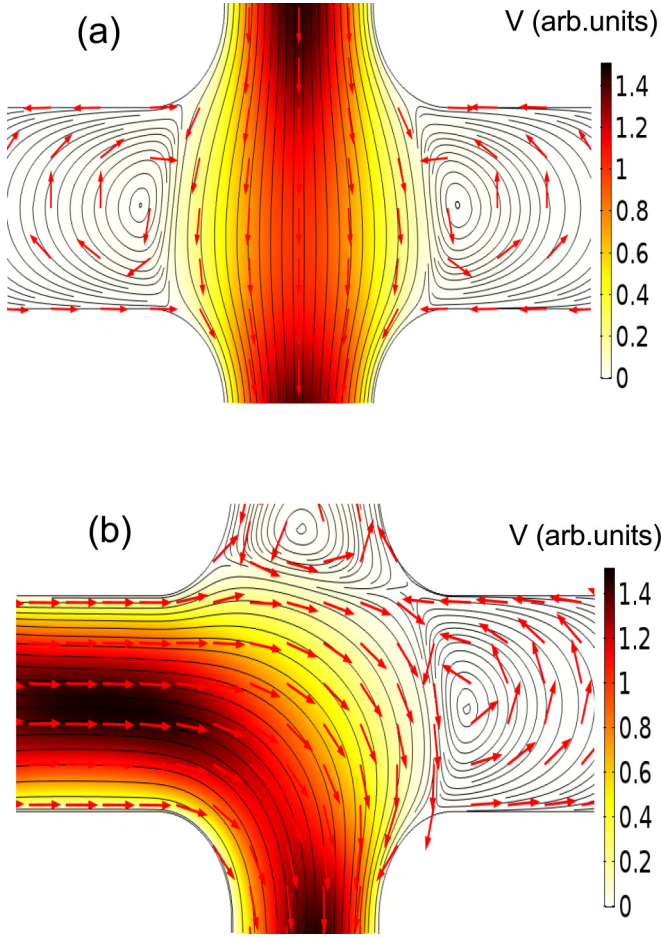


FIG. 1. Sketch of the different transport setup measurements, showing a velocity flow profile. (a) Nonlocal transport setup, proposed in [8]. (b) Nonlocal (vicinity) transport setup, proposed in [8–11].

experimental results. A good qualitative agreement between experimental and simulated data has been obtained.

II. NEGATIVE GIANT MAGNETORESISTANCE, EXPERIMENT, AND DISCUSSION

Our samples are high-quality, GaAs quantum wells with a width of 14 nm. Parameters characterizing the electron system are given in Table I. We present experimental results on Hall-bar devices designed in two different configurations. Design I consists of three $5\ \mu\text{m}$ wide consecutive segments of different length (10, 20, $10\ \mu\text{m}$), and eight voltage probes. Figure 2(top) shows the image of a typical multiprobe Hall device I. Design II is also a Hall bar with three $2\ \mu\text{m}$ wide

TABLE I. Parameters of the electron system in a mesoscopic samples at $T = 1.4\ \text{K}$. Parameters are defined in the text.

W (μm)	n_s ($10^{11}\ \text{cm}^{-2}$)	v_F ($10^7\ \text{cm/s}$)	l (μm)	l_2 (μm)	η (m^2/s)
5	9.1	4.1	40	2.8	0.3
2	6.0	3.3	20.6	1.4	0.12

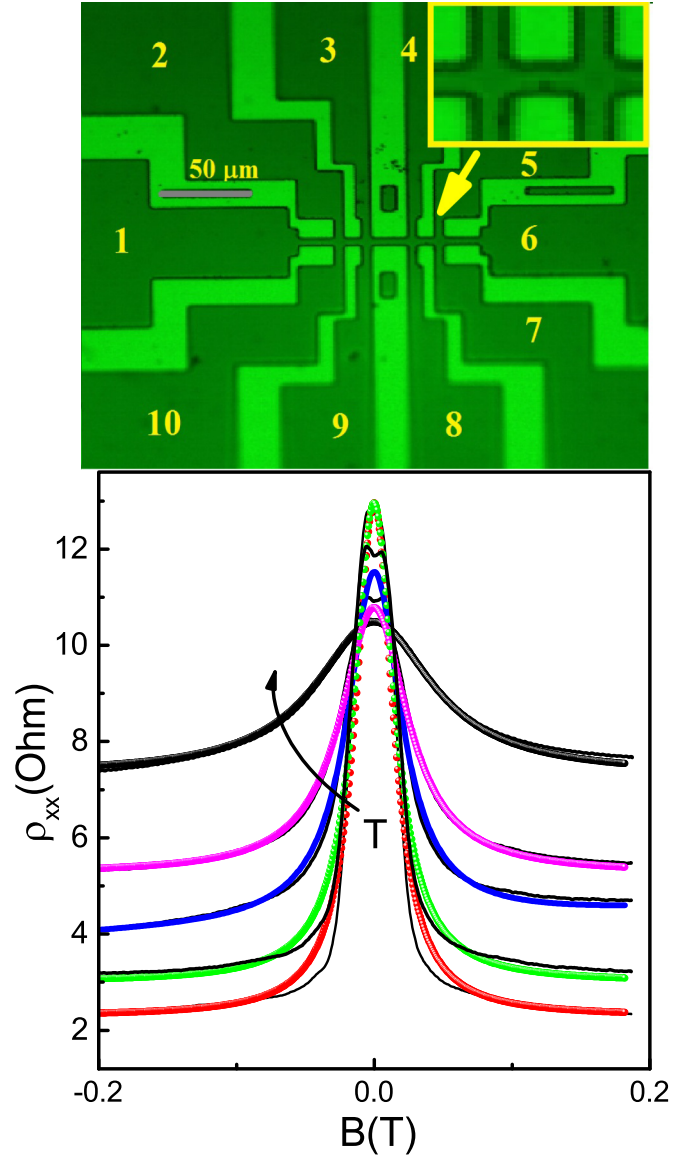


FIG. 2. Top: Image of the Hall-bar device. Top right: Zoomed Hall-bar bridge. Temperature dependent magnetoresistance of a GaAs quantum well in a Hall bar sample $W = 5\ \mu\text{m}$. Thick lines are examples illustrating magnetoresistance calculated from Eqs. (1) and (2) for different temperatures: 4.2 K (red), 14 K (green), 19 K (blue), 26 K (magenta), and 37.1 K (black).

consecutive segments of different length (2, 7, $2\ \mu\text{m}$), and eight voltage probes. The measurements were carried out in a VTI cryostat, using a conventional lock-in technique to measure the longitudinal ρ_{xx} resistivity with an ac current of $0.1\text{--}1\ \mu\text{A}$ through the sample, which is sufficiently low to avoid overheating effects. Five Hall bars from two different wafers were studied.

Longitudinal magnetoresistance has been studied in previous research for different configurations of the current and voltage probes [16]. Before analyzing the nonlocal effect and in order to make this analysis more complete, we present the results of measurements of the longitudinal magnetoresistivity $\rho_{xx}(B)$. Figure 2(a) shows $\rho_{xx}(B)$ as a function of magnetic field and temperature. One can see two characteristic

features: a giant negative magnetoresistance ($\sim 400\%$ – 600%) with a Lorentzian-like shape, and a pronounced temperature dependence on zero field resistance. In the hydrodynamic approach, the semiclassical treatment of the transport describes the motion of carriers when the higher order moments of the distribution function are taken into account. The momentum relaxation rate $1/\tau$ is determined by electron interaction with phonons and static defects (boundary). The second moment relaxation rate $1/\tau_{2,ee}$ leads to the viscosity and contains the contribution from the electron-electron scattering and temperature independent scattering by disorder [12,13]. It has been shown that conductivity obeys the additive relation and is determined by two independent *parallel* channels: the first is due to momentum relaxation time and the second due to viscosity [12,13]. This approach allows the introduction of the magnetic field dependent viscosity tensor and the derivation of the magnetoresisivity tensor [12–15]:

$$\rho_{xx} = \rho_0^{\text{bulk}} \left(1 + \frac{\tau}{\tau^*} \frac{1}{1 + (2\omega_c \tau_{2,ee})^2} \right), \quad (1)$$

where $\rho_0^{\text{bulk}} = m/n e^2 \tau$, $\tau^* = \frac{W(W+6l_s)}{12\eta}$, viscosity $\eta = \frac{1}{4} v_F^2 \tau_{2,ee}$.

We also collect the equations for relaxation rates separately:

$$\frac{1}{\tau_{2,ee}(T)} = A_{ee}^{FL} \frac{T^2}{[\ln(E_F/T)]^2} + \frac{1}{\tau_{2,0}}, \quad (2)$$

where E_F is the Fermi energy, and the coefficient A_{ee}^{FL} can be expressed via the Landau interaction parameter, however, it is difficult to calculate quantitatively (see discussion in [12]). The relaxation rate $\frac{1}{\tau_{2,0}}$ is not related to the electron-electron collisions, since any process responsible for relaxation of the second moment of the distribution function, even scattering by static defect, gives rise to viscosity [12]. A logarithmic factor is also present in the expression for quantum lifetime of weakly interacting 2D gas due to electron-electron scattering [17]:

$$\frac{\hbar}{\tau_{0,ee}(T)} = A_{ee}^0 \frac{T^2 [\ln(2E_F/T)]}{E_F} + \frac{\hbar}{\tau_{2,0}}, \quad (3)$$

where A_{ee}^0 is a numerical constant of the order of unity. Note, however, that since the relaxation time $\tau_{0,ee}$ is related to the kinematic of the electron-electron collisions, Expression (2) is more convenient and it is preferable to use. Finally, it has been shown that due to the disorder assisted contribution to the relaxation rate of the second moment of the distribution function, the expression is rewritten as

$$\frac{1}{\tau_{2,ee}^{da}(T)} = A_{ee}^{da} T^2 + \frac{1}{\tau_{2,0}}, \quad (4)$$

where the coefficient A_{ee}^{da} depends on the disorder type and its strength [12]. The moment relaxation rate is expressed as

$$\frac{1}{\tau} = A_{\text{ph}} T + \frac{1}{\tau_0}, \quad (5)$$

where A_{ph} is the term responsible for the phonon scattering [18,19], and $\frac{1}{\tau_0}$ is the scattering rate due to static disorder (not related to the second moment relaxation rate $\frac{1}{\tau_{2,0}}$).

We fit the magnetoresistance curves in Fig. 2 and the resistance in zero magnetic field with the three

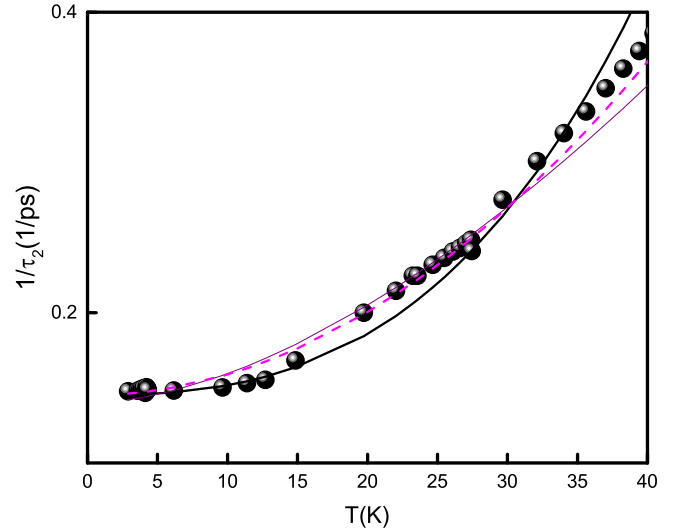


FIG. 3. Relaxation rate $1/\tau_2$ as a function of the temperature obtained by fitting the theory with experimental results $W = 5 \mu\text{m}$. Thick black line is Eq. (2), thin black line is Eq. (3), dashes are Eq. (4).

fitting parameters: $\tau(T)$, $\tau^*(T)$, and $\tau_{2,ee}(T)$. Figure 3 shows the dependencies of $1/\tau_{2,ee}(T)$ extracted from the comparison of the magnetoresistance shown in Fig. 2 and Eq. (1). We compare the temperature dependence of $\frac{1}{\tau_{2,ee}(T)}$ with theoretical predictions given by Eqs. (2)–(4) and present the results of such comparison in Fig. 3. The following parameters are extracted: $1/\tau_{2,0} = 1.45 \times 10^{11} \text{ s}^{-1}$, $A_{ee}^{FL} = 0.9 \times 10^9 \text{ s}^{-1} \text{ K}^{-2}$, $A_{ee}^0 = 1.3$, $A_{ee}^{da} = 2.0 \times 10^{10} \text{ s}^{-1} \text{ K}^{-2}$. All theoretical curves demonstrate reasonable agreement within experimental uncertainty. Hence, these mechanisms lead to nearly equivalent results and cannot be unambiguously distinguished based only on the temperature dependence of the relaxation time. Note that analysis of the nonlocal effect, considered below, does not depend on the relaxation mechanism.

In addition, we extract the temperature dependence of the moment scattering rate and determine parameters $A_{\text{ph}} = 10^9 \text{ s K}^{-1}$ and $\tau_0 = 5 \times 10^{-10} \text{ s}$, which are correlated with previous studies [17,18]. Relaxation time $\tau^*(T)$ depends on the $\tau_{2,ee}(T)$ and boundary slip length l_s . Comparing these values, we find that $l_s = 3.2 \mu\text{m} < L$, and, therefore, in our case, it is appropriate to use diffusive boundary conditions. Table I shows the mean free paths $l = v_F \tau$, $l_2 = v_F \tau_{2,ee}$, and viscosity, calculated with parameters extracted from the fit of experimental data.

III. EXPERIMENT: NONLOCAL RESISTANCE

In this section we focus on the nonlocal configurations because such geometry facilitates the observation of current whirlpools. Figure 4 shows the transport in a nonlocal setup, where the current is injected across the strip between probes 4 and 8. The voltage drop is measured between probes 5 and 7. Below we refer to it as C1 configuration. Poiseuille flow for a two-dimensional liquid is presented in Fig. 1(a). Note, however, that 2D charged liquid displays pronounced ballistic transport behavior. One can see strong oscillations

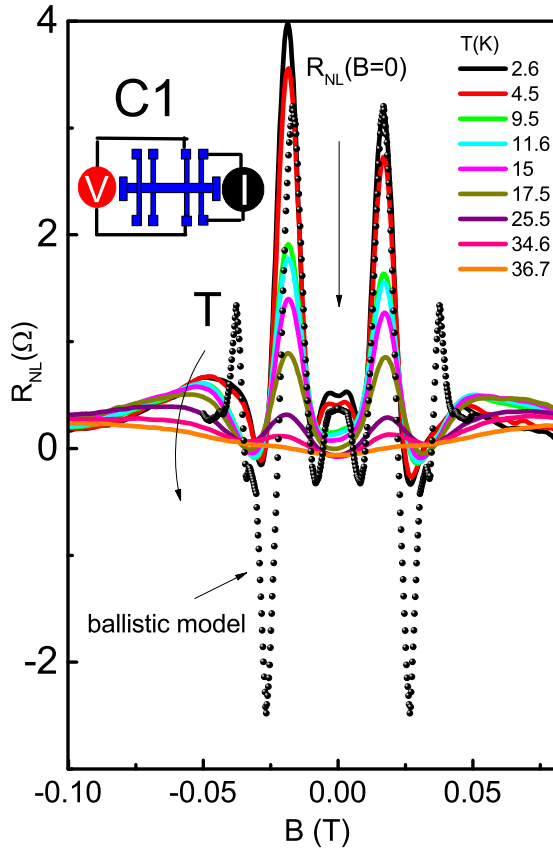


FIG. 4. Nonlocal transport signal versus magnetic field for different temperatures $W = 5 \mu\text{m}$. The dots represent results for the billiard model.

in weak magnetic fields due to geometrical resonance effects considered in the semiclassical billiard model [20,21]. We perform numerical simulations of the electron trajectories in ballistic structures. The results of these simulations (black dots) are compared to the experimental data. We observe an agreement with experimental data only at low magnetic field. Although the position of the resistance peaks at higher magnetic field coincide with calculations, the negative peak has a much smaller value, and the positive peak is wider than that obtained from the billiard model. Figure 4 also shows the evolution of the nonlocal magnetoresistance with temperature. One can see that all oscillations are smeared out by temperature and magnetoresistance at high temperature has a parabolic shape. Remarkably, the nonlocal resistance at $B = 0$ is positive at low temperatures, in accordance with the billiard model calculations, and then it changes sign and becomes negative at higher temperatures (Fig. 5). Figure 6 shows the transport in a nonlocal setup, where the current is injected between probes 1 and 8 and the voltage is measured between probes 5 and 6 (referred to as configuration C2). The Poiseuille flow for a two-dimensional liquid is presented in Fig. 1(b). As in configuration C1, one can see strong oscillations due to the geometrical resonance effect. Note that the ballistic transport in this configuration is very well established and studied previously in numerous publications [20,21]. In cross junction geometry, it was denominated as bend resistance [21]. We also perform the classical simulations for the transport

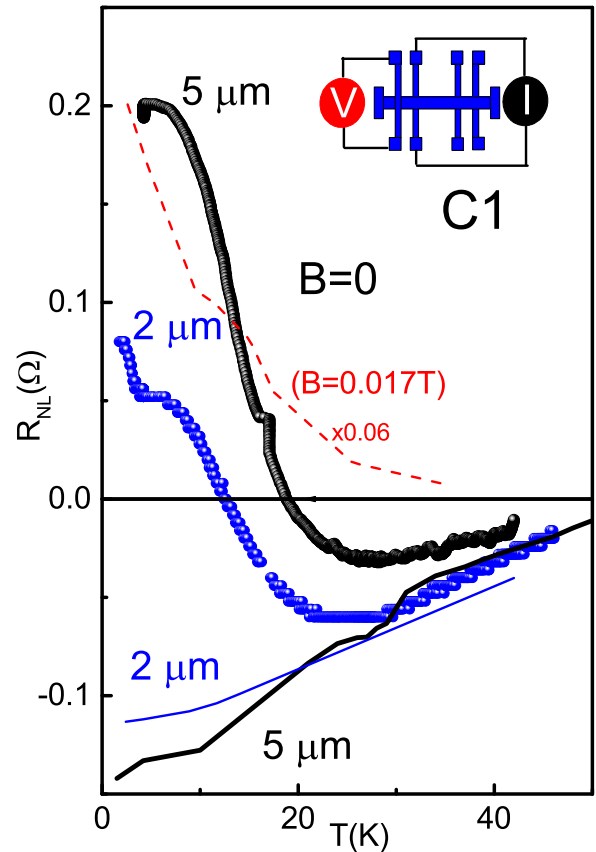


FIG. 5. T dependence of the nonlocal signal for different sample configurations. Solid lines show the calculations from Eq. (6) for $x = 10 \mu\text{m}$ ($W = 5 \mu\text{m}$) and $x = 5 \mu\text{m}$ ($W = 2 \mu\text{m}$). Dashes: T dependence of the ballistic peak at $B = 0.017T$.

in configuration C2, and the results are displayed in Fig. 6. Note, however, that in contrast to configuration C1, the bend resistance reveals a strong negative resistance peak near zero magnetic field [21,22]. This peak may mask the negative nonlocal signal due to viscosity, and detailed comparison is required to examine the significance of the hydrodynamic effect at low and high temperatures. Figure 7 presents the results of the nonlocal resistance temperature measurements in configuration C2 in zero magnetic field. One can see that the signal dramatically drops to zero in the $W = 5 \mu\text{m}$ sample, and resistance changes sign at high temperature in the $W = 2 \mu\text{m}$ sample. We also used a similar voltage measurement setup, where the current is injected between probes 1 and 8 and the voltage is measured between probes 4 and 5 (referred to as configuration C3). The nonlocal resistance in configuration C3 at zero magnetic field is shown in Fig. 7 for both samples designs.

IV. THEORY AND DISCUSSION

As has been shown in the previous section the viscosity leads to the incorporation of an extra relaxation mechanism [12–15] in zero magnetic field: $\rho = \rho_0^{\text{bulk}}(1 + \frac{\tau}{\tau^*})$. The dominant viscous contribution to resistivity corresponds to the small ratio between relaxation of the second moment of the electron distribution function and the first moment $\tau^*/\tau \ll 1$.

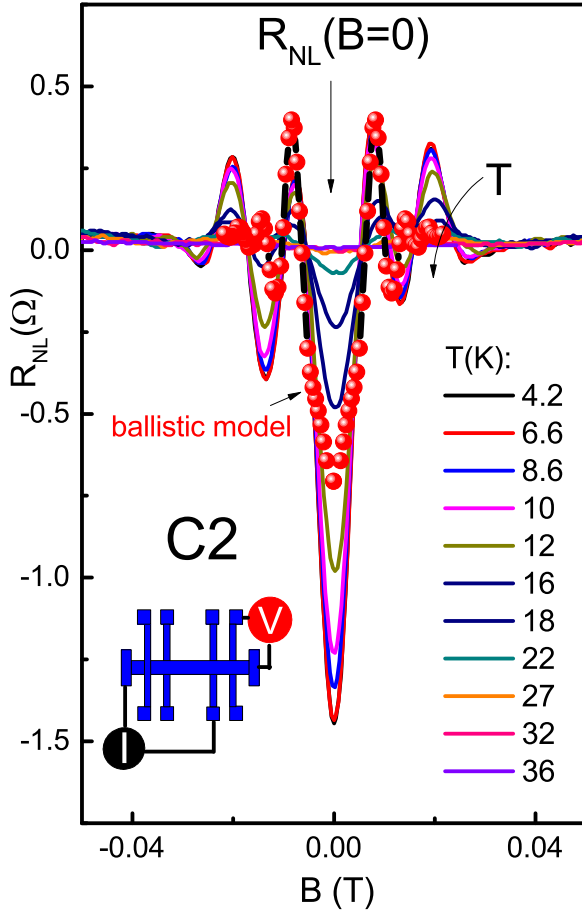


FIG. 6. Nonlocal transport signal versus magnetic field for different temperatures $W = 5 \mu\text{m}$. The dots represent results for the billiard model.

Comparative analysis between nonlocal geometries C1 and C2 demonstrates a qualitative difference. Crucially, the experimental observation of swirling features depends on the parameters that affect the spacial distribution of the two-dimensional potential inside the viscous charge flow. The first parameter is the boundary slip length l_s . The boundary no-slip conditions correspond to the ideal hydrodynamic case of diffusive boundaries with $l_s = 0$. It has been shown that the negative nonlocal signal is robust to boundary conditions [10]. For example, the Gurzhi effect disappears for free surface boundary conditions ($l_s = \infty$), while whirlpools in hydrodynamic electron flow, and the resulting negative nonlocal response, do exist. The second parameter which drastically affects whirlpool behavior is the vorticity diffusion length $D_\eta = \sqrt{\eta\tau}$. Figure 8 represents the temperature dependence of characteristic lengths in a $W = 5 \mu\text{m}$ sample. Previous studies have not investigated whether typically developed current whirlpools show sensitivity to the geometry and confinement effect [8–10]. However, the careful inspection of theoretical results [9] reveals that geometry C1 exhibits the occurrence of whirlpools only above the threshold value of $D_\eta = 0.225W$ (Fig. 8). The vicinity geometry C2, which is shown in Fig. 1(b), by contrast, allows the formation of current whirlpools for arbitrary small values of D_η , but only in very close proximity

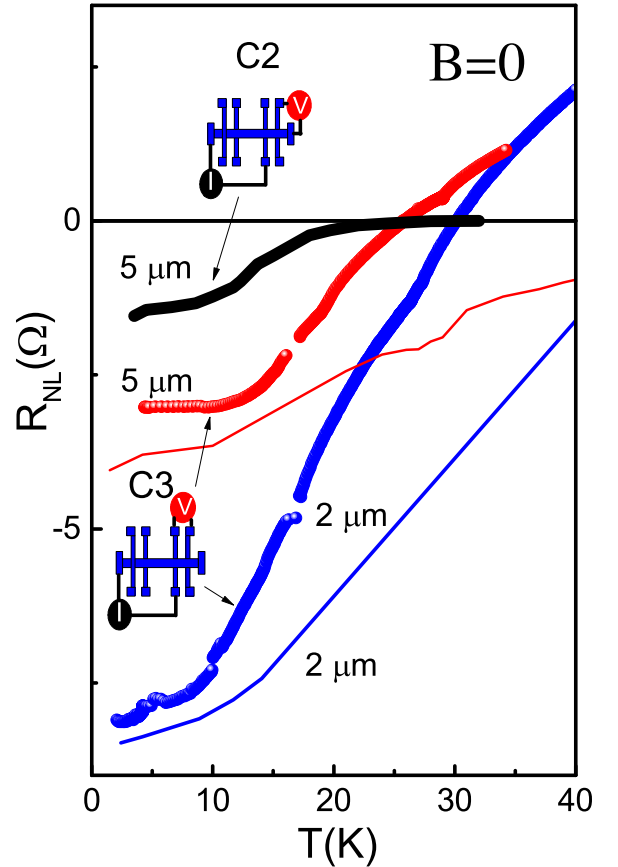


FIG. 7. T dependence of the nonlocal signal for different sample configurations. Thin solid lines show the calculations from Eq. (7) for $x = 3 \mu\text{m}$ ($W = 5 \mu\text{m}$) and $x = 1.5 \mu\text{m}$ ($W = 2 \mu\text{m}$).

to the current injector probe [10]. However, the value of D_η affects the spatial extension of the whirlpools, therefore, a high viscosity system facilitates observation of the negative vicinity resistance for a voltage detector placed at a large distance from the current injection probe. Moreover, the ballistic effect may induce the negative vicinity signal [19] and, therefore, requires more careful qualitative analysis. In the previous section we show the temperature dependence of low field magnetoresistance as well as the electrical resistivity over a temperature range extending from 1.7 to 40 K and obtain variation of the viscosity time with temperature. We use this data to estimate the nonlocal signal in our samples. The models [8–10] predict negative nonlocal resistance in configuration C1 at the distance $\bar{x} = \pi x/W$ from the main current path in the limits of free surface boundary conditions ($l_s = \infty$) in zero magnetic field:

$$R_{\text{NL}}^{\text{C1}} = -\rho_0 \left\{ \frac{\ln[\tanh^2(\bar{x}/2)]}{\pi} + 4\pi \left(\frac{D_v}{W} \right)^2 \frac{\cosh(\bar{x})}{\sinh^2(\bar{x})} \right\}. \quad (6)$$

In contrast to configuration C1, the results for vicinity geometry can be simplified only in the limit where the distance between the current injection probe is infinite:

$$R_{\text{NL}}^{\text{C2}} = -\frac{\rho_0}{2} \left\{ \frac{\ln[4T]}{\pi} - \frac{\bar{x}}{W} + \pi \left(\frac{D_v}{W} \right)^2 \frac{1}{T} \right\}, \quad (7)$$

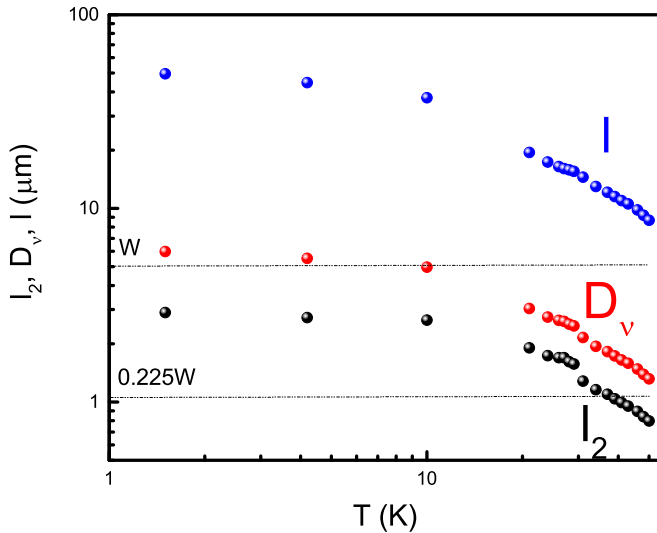


FIG. 8. The characteristic parameters as a function of the temperature for the sample with width $W = 5 \mu\text{m}$. The whirlpool threshold is indicated by the dashes.

where $\mathcal{T} = \sinh^2(\bar{x}/2)$. Figure 9 shows the nonlocal resistances in both configurations as a function of distance between voltage probe and current injector \bar{x} calculated from Eqs. (6) and (7) with parameters independently extracted from the local magnetoresistance measurements at $T = 4.2 \text{ K}$. For visualization of the data in the negative range, we used an absolute log scale. We observe that the magnitudes of nonlocal signals exhibit a universally exponential decay with distance from the current injector. Note that the nonlocal resistance is much stronger for geometry C1. The advantage of configuration C1 is that the ballistic contribution is positive and, therefore, it can be unambiguously discriminated from the negative viscous contribution. The calculated temperature dependence of $R_{\text{NL}}^{\text{C1}}$ is shown in Fig. 5 for $x = 10 \mu\text{m}$ ($W = 5 \mu\text{m}$) and $x = 5 \mu\text{m}$ ($W = 2 \mu\text{m}$), which roughly correspond to the distance between the center of the probes. Note that the ballistic contribution to the transport also depends on the temperature due to the thermal broadening of the Fermi distribution function and scattering by the phonons. A rough estimate of the nonlocal ballistic resistance temperature dependence for $L < l$ may be obtained using the formula $R_{\text{NL}} \sim \exp(-L/l)$, where L is the distance between probes [23]. Figure 5 shows the T dependence of the ballistic peak at $B = 0.017T$. One can see a rapid decrease of the peak with temperature. Therefore, the negative nonlocal resistance in zero field and at high temperature can be attributed only to hydrodynamic effects.

We also compare predictions for configurations C2 and C3 with experimental results. Note that we normalized ballistic resistance for the peak value at $B = 0.008T$ (Fig. 6), which we found more reliable, since this peak weakly depends on the boundary conditions and sample geometry [20]. The residual contribution at zero magnetic field could be due to viscous effects. In general, the ballistic contribution alone can explain the temperature dependence in zero field, below 20 K, without taking into account the viscous term. Above $T = 20 \text{ K}$, ballistic contribution should be exponentially small (see Fig. 5).

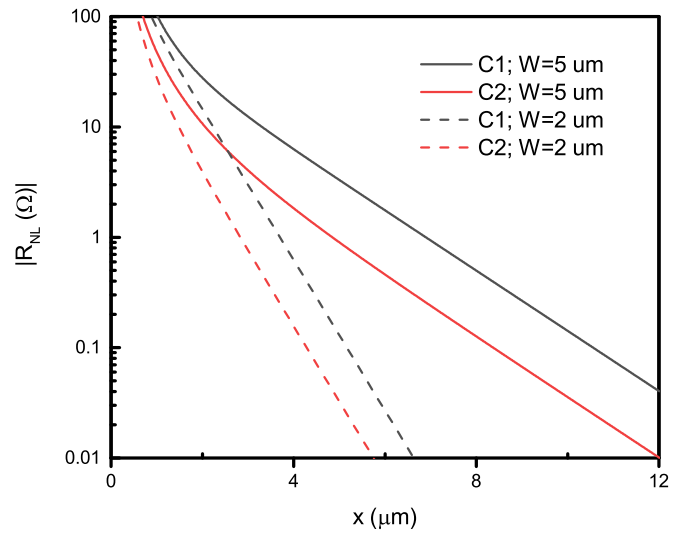


FIG. 9. The absolute value of the nonlocal resistance for two configurations as a function of the distance from the injector electrode $T = 4.2 \text{ K}$, parameters are determined from local magnetoresistance measurements.

Figure 7 shows the calculations from Eq. (7). Note that the analytical formula has been derived under several assumptions and we can apply the formula just for the evaluation of the upper limits of the signal. Figure 7 presents the results of such calculations. One can see that the predicted signal agrees with experimental data for $x = 3 \mu\text{m}$ ($W = 5 \mu\text{m}$) and $x = 1.5 \mu\text{m}$ ($W = 2 \mu\text{m}$), which roughly correspond to the distance between the centers of the probes. Note that, in a realistic sample, the width of the probes is comparable with the sample width W , while the theory considers $x \ll W$, also indicating the approximate character of the calculation. We may conclude here that geometry C1 exhibits a direct relation between the negative signal and formation of the current whirlpools. In geometries C2 and C3, negative nonlocal resistance follows the hydrodynamic predictions up to 30 K, however, it is very likely that the ballistic contribution is comparable or bigger than the hydrodynamic one at low temperatures. Above 30 K we observe a positive signal, which disagrees with both ballistic and hydrodynamic predictions. We attribute this behavior to approaching the condition $D_\eta = 0.225W$. Note that the observation of negative vicinity nonlocal resistance in graphene [11] requires more careful inspection of the ballistic contribution. Moreover, the condition $D_\eta = 0.225W$ is not fully completed (see also discussion in [10]), therefore, our observation of the negative nonlocal resistance in geometry C1 provides more clear evidence of current vortices. It is important to note that the transport signatures of the viscosity in the nonlocal effect are correlated in our samples with other observations, such as a giant longitudinal magnetoresistance and the Gurzhi effect [16].

V. SUMMARY AND CONCLUSIONS

In conclusion, we have studied nonlocal transport in a mesoscopic two-dimensional electron system in terms of viscosity of the fluids. In contrast to the Ohmic flow of the

particles, viscous flow can result in a backflow of the current and negative nonlocal voltage. We have measured voltage in different arrangements of current and voltage contacts and found a negative response, which we attributed to the formation of current whirlpools. Nonlocal viscosity-induced transport is strongly correlated with observations of the Gurzhi effect

and low magnetic field transport described by hydrodynamic theory.

ACKNOWLEDGMENTS

The financial support of this work by the Russian Science Foundation (Grant No.16-12-10041), FAPESP (Brazil), and CNPq (Brazil) is acknowledged.

-
- [1] S. Conti and G. Vignale, *Phys. Rev. B* **60**, 7966 (1999).
 - [2] R. N. Gurzhi, *Sov. Phys. Usp.* **11**, 255 (1968); R. N. Gurzhi, A. N. Kalinenko, and A. I. Kopeliovich, *Phys. Rev. Lett.* **74**, 3872 (1995).
 - [3] M. Dyakonov and M. Shur, *Phys. Rev. Lett.* **71**, 2465 (1993).
 - [4] M. I. Dyakonov and M. S. Shur, *Phys. Rev. B* **51**, 14341 (1995).
 - [5] M. Dyakonov and M. Shur, *IEEE Trans. Electron Devices* **43**, 380 (1996).
 - [6] A. O. Govorov and J. J. Heremans, *Phys. Rev. Lett.* **92**, 026803 (2004).
 - [7] L. W. Molenkamp and M. J. M. de Jong, *Solid-State Electron.* **37**, 551 (1994); M. J. M. de Jong and L. W. Molenkamp, *Phys. Rev. B* **51**, 13389 (1995).
 - [8] L. Levitov and G. Falkovich, *Nat. Phys.* **12**, 672 (2016).
 - [9] I. Torre, A. Tomadin, A. K. Geim, and M. Polini, *Phys. Rev. B* **92**, 165433 (2015).
 - [10] F. M. D. Pellegrino, I. Torre, A. K. Geim, and M. Polini, *Phys. Rev. B* **94**, 155414 (2016).
 - [11] D. A. Bandurin, I. Torre, R. K. Kumar, M. B. Shalom, A. Tomadin, A. Principi, G. H. Auton, E. Khestanova, K. S. Novoselov, I. V. Grigorieva, L. A. Ponomarenko, A. K. Geim, and M. Polini, *Science* **351**, 1055 (2016).
 - [12] P. S. Alekseev, *Phys. Rev. Lett.* **117**, 166601 (2016).
 - [13] T. Scaffidi, N. Nandi, B. Schmidt, and A. P. Mackenzie, and J. E. Moore, *Phys. Rev. Lett.* **118**, 226601 (2017).
 - [14] L. V. Delacretaz and A. Gromov, *Phys. Rev. Lett.* **119**, 226602 (2017).
 - [15] F. M. D. Pellegrino, I. Torre, and M. Polini, *Phys. Rev. B* **96**, 195401 (2017).
 - [16] G. M. Gusev, A. D. Levin, E. V. Levinson, and A. K. Bakarov, *AIP Adv.* **8**, 025318 (2018).
 - [17] Z. Qian and G. Vignale, *Phys. Rev. B* **71**, 075112 (2005).
 - [18] J. J. Harris, C. T. Foxon, D. Hilton, J. Hewett, C. Roberts, and S. Auzoux, *Surface Science* **229**, 113 (1990).
 - [19] T. Kawamura and S. Das Sarma, *Phys. Rev. B* **45**, 3612 (1992).
 - [20] C. W. J. Beenakker and H. van Houten, *Phys. Rev. Lett.* **63**, 1857 (1989).
 - [21] M. L. Roukes, A. Scherer, S. J. Allen, Jr., H. G. Craighead, R. M. Ruthen, E. D. Beebe, and J. P. Harbison, *Phys. Rev. Lett.* **59**, 3011 (1987).
 - [22] G. Timp, H. U. Baranger, P. de Vegvar, J. E. Cunningham, R. E. Howard, R. Behringer, and P. M. Mankiewich, *Phys. Rev. Lett.* **60**, 2081 (1988).
 - [23] Y. Hirayama and S. Tarusha, *Appl. Phys. Lett.* **63**, 2366 (1993).